DOI 10.1007/s11204-018-9495-3
Soil Mechanics and Foundation Engineering, Vol. 55, No. 1, March, 2018 (Russian Original No. 1, January-February, 2018)

SOIL MECHANICS

EFFECT OF HYDRAULIC PRESSURE AND TECTONIC STRESS ON FRACTURE INITIATION IN ROCK FLAWS

UDC 620.192:624.131.52

Linfei Zhang[1], Qingwen Ren[2], Mei Tao[2], Qiang Tong[2]
[1]College of Water Conservancy and Hydropower Engineering, Hohai University, Nanjing, PR China; [2]College of Mechanics and Materials, Hohai University, Nanjin, PR China.

This study examines the effects of hydraulic pressure and tectonic stress on fracture initiation in rock flaws by using the finite element method. A square domain with double flaws is analyzed under vertical load, different horizontal loads (modeling tectonic stresses), and various hydraulic pressures.

Introduction

Crack initiation and propagation in solid under water pressure is called hydraulic fracturing. Hydraulic fracturing technology has been extensively applied in engineering, including the measurement of in situ stresses [1], stimulation of groundwater wells [2], and solid waste disposal [3]. The hydraulic fracturing mechanism has been extensively studied to improve the hydraulic fracturing design for engineering applications and avoid hydraulic fracturing for engineering safety. The literature shows that the orientation of new fractures is influenced by several factors, such as local stress field [4], geometry of existing fractures [5-6], anisotropy of the rock [7], and ratio between vertical load and hydraulic pressure [8]. However, the propagation direction of newly created fractures and the failure mechanism remain unclear.

Numerous laboratory experiments under uniaxial and biaxial loading conditions [7, 9], have been performed to gain insights into fracturing mechanisms. Numerical methods are generally suitable for the examination of rock fracturing behaviors with general geometries and loading conditions. The finite element method (FEM) [8, 10], XFEM [11, 12], RFPA [13], PFC [14, 15], DDA [16], NMM [17], BEM [18], and other methods [19, 20] have been adopted to investigate the fracturing mechanisms in rocks. However, systematic studies on vertical load and hydraulic pressure in existing flaws under different tectonic stresses are limited. In the present article we carried out an in-depth investigation of the effects of hydraulic pressure and tectonic stress on fracture initiation in rock flaws by numerical simulation. The maximum principal stress and maximum shear stress along the flaw perimeter, which are related to fracture initiation, were evaluated.

Methodology

The stress field is numerically investigated by elastic FEM in ABAQUS to systematically examine the effect of horizontal load and hydraulic pressure applied in existing flaws on the stress field along the flaw perimeters, especially in the vicinity of the flaw tips. The material of the model is considered

Translated from Osnovaniya, Fundamenty i Mekhanika Gruntov, No. 1, pp. 9-13, January-February, 2018.
0038-0741/18/5501-0009

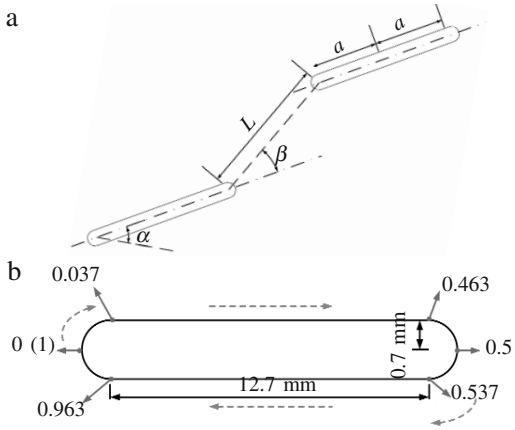

Fig. 1. Geometry of a double flaw (a) and definition of the normalized position along the flaw perimeter (b).

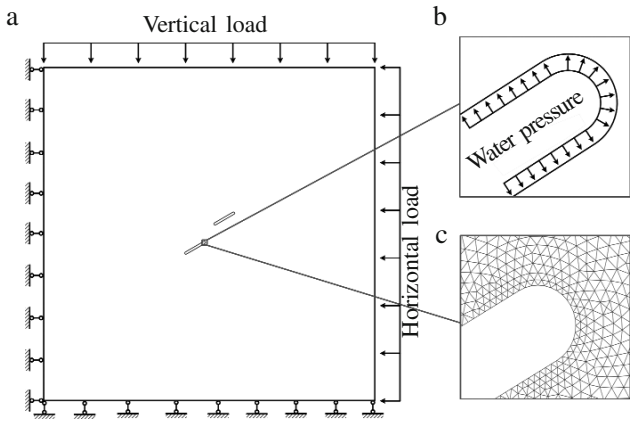

Fig. 2. Boundary conditions and loads (a), details of the flaws with water pressure (b), and of the finite element mesh near one of the flaw tips (c).

continuous, homogeneous, and isotropic linear elastic. The material parameters are as follows: Young's modulus 6 GPa and Poison's ratio 0.28 [9, 21].

Figure 1(a) shows the geometry of a double flaw. The lengths of two flaws are the same, and the half flaw length a is 6.35 mm, $L = 2a$, and $\alpha = \beta = 30°$. Figure 1(b) shows other parameters of a single flaw.

A 20 cm wide square domain with double flaws (Fig. 1) is analyzed. Figure 2(a) presents the boundary conditions and loads. Three different types of loads, namely, a vertical load (VL) applied at the top boundary, a horizontal load (HL) applied at the right boundary of the numerical model, and a water pressure (WP) applied along the surface of the flaws, are considered, as shown in Figs. 2(a) and 2(b). The vertical load is 10 MPa, the horizontal load varies from 0 to 40 MPa, and three water pressures are selected, namely, 0 MPa (without water pressure), 15 MPa (relatively small water pressure), and 30 MPa (relatively large water pressure). The ratio k = WP/VL and the lateral pressure coefficient λ = HL/VL are defined. Table 1 shows the vertical load and horizontal load cases for each k. The λ studied intends to a simulate tectonic stress field. The finite elements in the numerical analysis are three-node linear plane stress triangles. The finite element mesh around the flaws is shown in Fig. 2(c). The present study adopts two stress-based initiation criteria, namely, maximum principal stress and maximum shear stress [9].

TABLE 1

HL, MPa	VL, MPa	λ = HL/VL
0	10	0.0
2.8	10	0.3
6	10	0.6
10	10	1.0
20	10	2.0
30	10	3.0
40	10	4.0

The left flaw will be analyzed in detail. The one-dimensional normalized position along the flaw perimeter is defined as follows to conveniently express the results along the flaw face: (1) the origin is located at the left flaw tip; (2) the ratio of the distance from the considered point to the origin and the entire flaw circumference is defined as a normalized position; and (3) normalized positions along the flaw perimeter are defined clockwise. The normalized position varies from 0 to 1, as shown in Fig. 1(b). This path is similar to that shown in [22]. Goncalves da Silva [23] studied other paths around the flaw tip and found that the variation in paths does not significantly affect the fracture initiation results obtained.

Numerical results

The evolution of maximum principal stresses along the flaw perimeter for several typical λ without water pressure is shown in Fig. 3(a). As λ increases from 0 to 1.0, the peak of maximum principal stresses decreases, and the location of the peak moves from 0.47 to 0.42. Notably, maximum principal stresses rapidly decrease when the peak location is closer to 0.5 for each λ. As λ increases from 1.0 to 3.0, compressive stresses appear on the small semicircular spot of the flaw tip and presents a gradually increasing trend. The maximum principal stress is zero everywhere else around the flaw. As λ increases from 3.0 to 4.0, the peak of maximum principal stresses gradually increases, and the peak location moves from 0.54 to 0.53. This result indicates that the position of a tensile fracture not only relies on the vertical load (constant load in this paper) but also on the horizontal load, especially when $\lambda < 1.0$ and $\lambda > 3.0$.

The following conclusions can also be drawn from Fig. 3(a): (1) the peak of the maximum principal stresses with approximately 22.7 MPa for λ is higher than that with approximately 3.4 MPa for $\lambda = 0.6$, but the peak of the maximum principal stresses with approximately 1.0 MPa for $\lambda = 3.0$ is lower than that with approximately 9.7 MPa for $\lambda = 4.0$ In other λ cases, the maximum principal stress is nearly equal to that of compressive stress or zero. Theoretically, initiation of new tensile fractures may definitely be related to λ; (2) the maximum principal stress is nearly 0 MPa at the region from 0.58 to 0.64 and from 0.08 to 0.14 for all λ.

The evolution of maximum shear stresses along the flaw perimeter for several typical λ with $k = 0$ is shown in Fig. 3(b). As λ increases from 0 to 1.0, the peak location moves from 0.51 to 0.50. As λ increases from 1.6 to 4.0, the peak of maximum principal stresses presents a gradually increasing trend, and the peak location is approximately 0.48. This result indicates that the position of a shear fracture is divided into two main sections with increasing λ. The peak of the maximum shear stresses remains approximately 31.5 MPa as λ increases from 0 to 1.0; the peak of the maximum shear stresses varies from 46.7 MPa to 93.6 MPa as λ increases from 2.0 to 4.0; (2) the maximum shear stresses at points 0.59 and 0.10 remain approximately 1.4 MPa under all λ (Fig. 3(b)).

The evolution of maximum principal stresses along the flaw perimeter for several typical λ with $k = 1.5$ is shown in Fig. 3(c). As λ increases from 0 to 1.0, the peak of maximum principal stresses rapidly decreases, and the peak location moves from 0.48 to 0.5. As λ increases from 1.0 to 4.0, the peak of maximum principal stresses presents a gradually increasing trend, and the peak location moves from 0.5 to 0.52. The peak of maximum principal stresses reaches the lowest value when $\lambda = 1.0$, and the peak location is 0.5. This result indicates that the position of a tensile fracture probably begins at

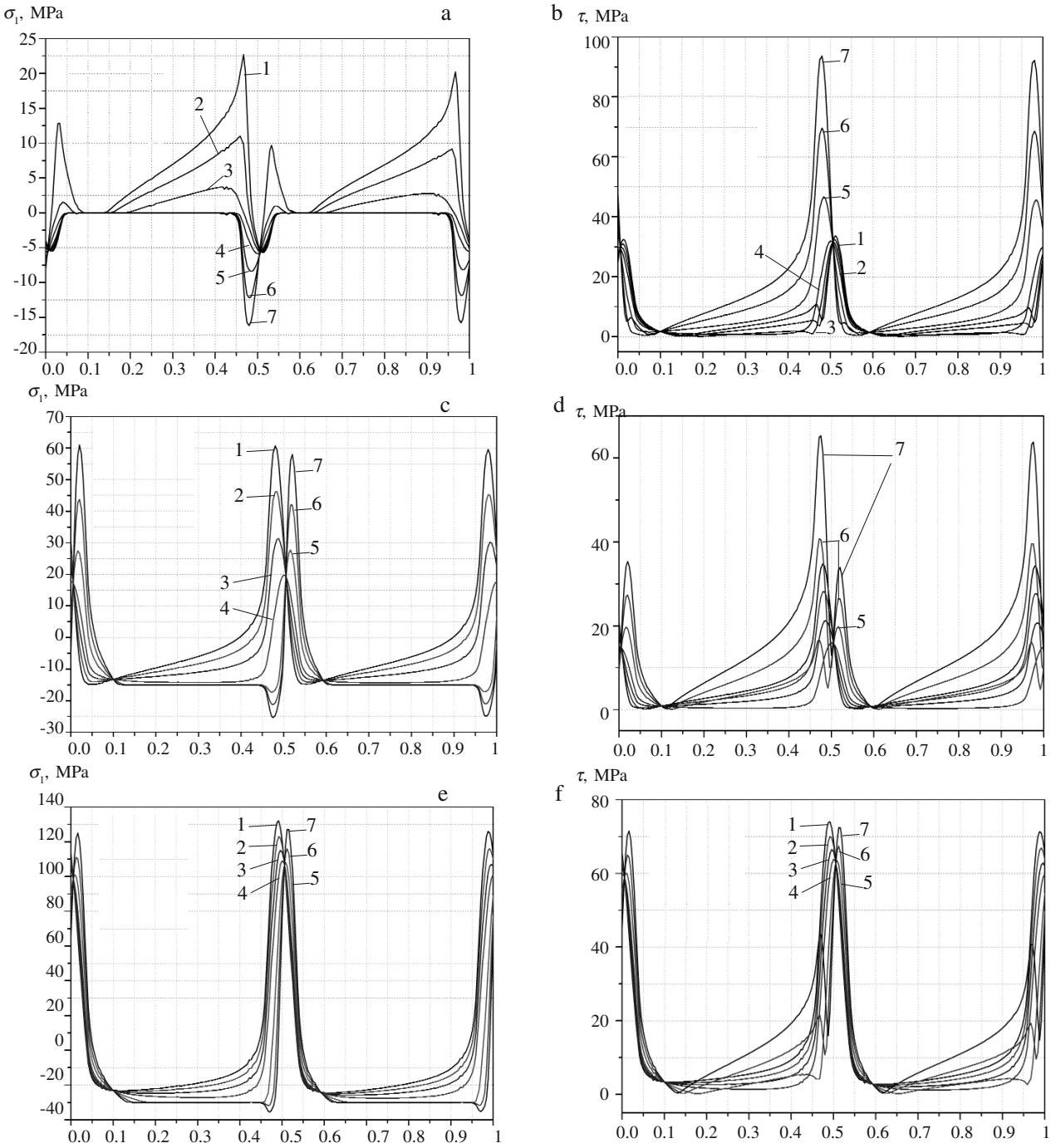

Fig. 3. Variations of (a) maximum principal stresses and (b) maximum shear stresses along the flaw perimeter for several typical λ: a) k = 0, b) k = 1.5, c) k = 3, 1) λ = 0, 2) λ = 0,28, 3) λ = 0,6, 4) λ = 1, 5) λ = 2, 6) λ = 3, 7) λ = 4.

the middle flaw tip for HL = VL. The peak of the maximum principal stresses decreases from 60.7 to 19.8 MPa as λ increases from 0 to 1.0, and the peak of the maximum principal stresses increases from 19.8 to 45.7 MPa as λ increases from 1.0 to 4.0. Theoretically, initiation of new tensile fractures may definitely be related to λ with k = 1.5; the maximum principal stresses at points 0.59 and 0.10 remain approximately 13.6 MPa under all λ.

TABLE 2

λ	k = 0		k = 1.50		k = 3.0	
	position	σ_1, MPa	position	σ_1, MPa	position	σ_1, MPa
0	0.467	22.7	0.480	60.7	0.492	131.7
0.28	0.459	11.0	0.484	46.3	0.492	122.9
0.6	0.422	3.4	0.488	31.3	0.496	115.3
1.0	-	-	0.500	19.8	0.500	109.4
2.0	-	-	0.516	27.7	0.508	108.2
3.0	0.541	1.0	0.520	42.0	0.512	116.2
4.0	0.533	9.7	0.529	45.7	0.516	126.8

TABLE 3

λ	k = 0		k = 1.50		k = 3.0	
	position	σ_1, MPa	position	σ_1, MPa	position	σ_1, MPa
0	0.967	20.2	0.980	59.6	0.988	125.9
0.28	0.959	9.1	0.980	45.2	0.992	116.3
0.6	0.927	2.7	0.984	30.2	0.996	107.5
1.0	-	-	0.000	17.7	0.000	100.8
2.0	-	-	0.016	27.5	0.008	100.8
3.0	0.041	1.5	0.021	43.8	0.012	111.2
4.0	0.033	12.9	0.021	61.0	0.016	125.0

TABLE 4

λ	k = 0		k = 1.50		k = 3.0	
	position	τ_{max}, MPa	position	τ_{max}, MPa	position	τ_{max}, MPa
0	0.512	33.7	0.480	34.8	0.492	74.0
0.28	0.508	32.3	0.484	28.1	0.492	70.0
0.6	0.508	31.5	0.488	21.2	0.496	66.5
1.0	0.500	31.9	0.500	16.0	0.500	63.8
2.0	0.484	46.7	0.516	19.8	0.508	63.5
3.0	0.480	69.6	0.471	40.8	0.512	67.4
4.0	0.480	93.6	0.475	65.3	0.512	72.4

TABLE 5

λ	k = 0		k = 1.50		k = 3.0	
	position	τ_{max}, MPa	position	τ_{max}, MPa	position	τ_{max}, MPa
0	0.012	32.5	0.980	34.3	0.988	71.4
0.28	0.012	31.0	0.980	27.7	0.992	66.9
0.6	0.008	29.8	0.984	20.7	0.996	62.8
1.0	1.000	29.9	1.000	15.0	1.000	59.9
2.0	0.984	45.7	0.016	19.7	0.008	60.1
3.0	0.980	68.6	0.971	39.6	0.012	65.0
4.0	0.980	92.2	0.975	63.8	0.016	71.6

The evolution of maximum shear stresses along the flaw perimeter for several typical λ with k = 1.5 is shown in Fig. 3(d). As λ increases from 0 to 1.0, the peak of the maximum shear stresses decreases, and the peak location moves from 0.48 to 0.5. As λ increases from 1.0 to 2.0, the peak of the maximum shear stresses slightly changes, but the peak location moves from 0.5 to 0.52. As λ increases from 2.0 to 4.0, the peak of the maximum shear stresses presents a gradually increasing trend, the peak location moves from 0.52 to 0.47, and the location of the maximum shear stresses is symmetrical at the position of 0.5.

Figure 3(d) shows the results of further analysis of the evolution of maximum shear stresses along the flaw perimeter. The peak of the maximum shear stresses changes from 38.4 to 21.2 MPa as λ increases from 0 to 1.0, and the peak of the maximum shear stresses changes from 19.8 to 65.3 MPa as λ increases from 2.0 to 4.0; (2) the maximum shear stresses at points 0.59 and 0.10 are approximately 0.7 MPa for all λ.

The evolution of maximum principal stresses along the flaw perimeter for several typical λ with k = 3.0 is shown in Fig. 3(e). As λ increases from 0 to 1.0, the peak of maximum principal stresses decreases, and the peak location moves from 0.49 to 0.5. As λ increases from 1.0 to 2.0, the peak of maximum principal stresses remains nearly constant, but the peak location moves from 0.5 to 0.51. As λ increases from 2.0 to 4.0, the peak of maximum principal stresses presents a gradually increasing trend, and the peak location moves from 0.5 to 0.52. The peak of the maximum principal stresses decreases from 131.7 MPa to 109.3 MPa as λ increases from 0 to 1.0, and the peak of the maximum principal stresses increases from 108.2 MPa to 126.8 MPa as λ increases from 2.0 to 4.0. This result indicates that under a relatively large water pressure, the horizontal load has minimal influence on the position of tensile crack initiation, and the maximum principal stresses at points 0.59 and 0.10 remain approximately 24.4 MPa for all λ.

The evolution of maximum shear stresses along the flaw perimeter for several typical λ with k = 3.0 is shown in Fig. 3(f). As λ increases from 0 to 1.0, the peak of maximum shear stresses decreases from 74.0 to 66.5 MPa, and the peak location moves from 0.49 to 0.50. As λ increases from 1.0 to 4.0, the peak of the maximum shear stresses increases from 63.8 to 72.4 MPa, and the corresponding location remains approximately 0.5. This result indicates that under a relatively large water pressure, the horizontal load has minimal influence on the position of shear crack initiation. The maximum shear stresses at points 0.59 and 0.10 remain approximately 2.8 MPa under all λ.

Notably, the tensile or shear crack initiation position is dependent on which material first reaches microscale strength [8]. Tables 2 to 5 summarize the positions of the fracture initiation that are only

applicable to maximum principal stresses or maximum shear stresses. Note that "-" denotes no tensile stress.

Conclusions

This study examined the effects of hydraulic pressure and tectonic stress on fracture initiation in rock flaws by using the elastic FEM in ABAQUS. Numerical results show the following:

1. As the lateral pressure coefficient λ increases without water pressure (k = 0), the initiation location of new tensile fractures moves from the position directly ahead of the flaw tip (0.47) to the upper face of the flaw (0.42), then from the lower face (0.54) to the position directly ahead of the flaw tip (0.53). Simultaneously, the initiation location of new shear fractures moves from the position directly ahead of the flaw tip (0.51) to the upper face (0.48). The positions of tensile and shearing fracture initiations depend on the horizontal load, especially when $\lambda < 1.0$ and $\lambda > 3.0$.

2. As λ increases with a relatively small water pressure (k = 1.5), the initiation location of new tensile fractures moves from the upper face of the flaw (0.48) to the lower face of the flaw (0.53). Simultaneously, the initiation location of new shear fractures moves from the upper face (0.48) to the lower face (0.52), then from the lower face (0.52) to the upper face (0.48). The positions of tensile and shearing fracture initiations depend on the horizontal load with a relatively small water pressure (k = 1.5).

3. Under a relatively large water pressure (k = 3.0), λ has minimal effect on the positions of tensile and shear fracture initiations but exhibit the same trend, and the positions of tensile and shear fracture initiations are directly ahead of the flaw tip (0.5).

4. Two interesting points exist, specifically at the lower face (0.59) and the upper face (0.10), where the maximum principal (shear) stress remains approximately constant for λ. Notably, the constant only relies on the water pressure.

The effects of hydraulic pressure and tectonic stress on propagation and coalescence of fractures warrant further study.

Acknowledgments

The research is supported by the National Natural Science Foundation of China (Grant No. 11132003 and No. 51739006) and the Project Funded by the Priority Academic Program Development of Jiangsu Higher Education Institutions.

REFERENCES

1. A. M. Raaen, E. Skomedal, H. Kjorholt, P. Markestad, and D. Okland, "Stress determination from hydraulic fracturing tests: the system stiffness approach," *Int. J. Rock Mech. Min. Sci*., **38**, 529-541 (2001).
2. L. C. Murdoch and W. W. Slack, "Forms of hydraulic fractures in shallow fine-grained formations," *Geotech. Geoenviron. Eng*., **128**, 479-487 (2002).
3. B. W. Hainey, R. G. Keck, M. B. Smith, K. W. Lynch, and J. W. Barth, "On-site fracturing disposal of oilfield-waste solids in Wilmington field," *SPE Prod. Facil.*, **14**, 83-87 (1999).
4. E. J. Nelson, J. J. Meyer, R. R. Hillis, and S. D. Mildren, "Transverse drilling induced tensile fractures in the West Tuna area, Gippsland Basin, Australia: implications for the in situ stress regime," *Int. J. Rock Mech. Min. Sci*., **42**, 361-371 (2005).
5. A. Bobet and H. H. Einstein, "Fracture coalescence in rock-type materials under uniaxial and biaxial compression," *Int. J. Rock Mech. Min. Sci.*, **35**, 863-888 (1998).
6. S. Q. Yang, Y. H. Huang, W. L. Tian, and J. B. Zhu, "An experimental investigation on strength, deformation and crack evolution behavior of sandstone containing two oval flaws under uniaxial compression," *Eng. Geol*., **217**, 35-48 (2017).
7. S. P. Morgan and H. H. Einstein, "Cracking Processes Affected by Bedding Planes in Opalinus Shale with Flaw Pairs," *Eng. Fract. Mech*., (2017), doi: http://dx.doi.org/10.1016/j.engfracmech.2017.03.003.
8. B. Goncalves da Silva and H. H. Einstein, "Finite Element study of fracture initiation in flaws subject to internal fluid pressure and vertical stress," *Int. J. Solids Struct*., **51**, 4122-4136 (2014).
9. A. Bobet, "Fracture Coalescence in Rock Materials: Experimental Observations and Numerical Predictions (Sc.D. thesis)," Massachusetts Institute of Technology (1997).
10. Y. Yao, "Linear elastic and cohesive fracture analysis to model hydraulic fracture in brittle and ductile rocks," *Rock Mech. Rock Eng*., **45**, 375-387(2012).

11. J. Rannou, N. Limodin, J. Rethore, A. Gravouil, W. Ludwig, M.-C.Baietto-Dubourg, J.-Y.Buffiere, A. Combescure, F. Hild, and S. Roux, "Three dimensional experimental and numerical multiscale analysis of a fatigue crack," *Comput. Methods Appl. Mech,* **199**, 1307-1325 (2010).
12. Z. Wang, T. T. Yu, T. Q. Bui, S. Tanaka, C. Z. Zhang, S. Hirose, and J. L. Curiel-Sosa, "3-D local mesh refinement XFEM with variable-node hexahedron elements for extraction of stress intensity factors of straight and curved planar cracks," *Comput. Methods Appl. Mech. Eng*., **313**, 375-405 (2017).
13. C. A. Tang, "Numerical simulation of progressive rock failure and associated seismicity," *Int. J. Rock Mech. Min*., **34**, 249-261 (1997).
14. D. O. Potyondy and P. A. Cundall, "A bonded-particle model for rock," *Int. J. Rock Mech. Min. Sci*., **41**, 1329-1364 (2004).
15. Y. H. Huang, S. Q. Yang, and J. Zhao, "Three-Dimensional Numerical Simulation on Triaxial Failure Mechanical Behavior of Rock-Like Specimen Containing Two Unparallel Fissures," R*ock Mech. Rock Eng*., **49**, 4711-4729 (2016).
16. C. J. Pearce, A. Thavalingam, Z. Liao, and N. Bicanic, "Computational aspects of the discontinuous deformation analysis framework for modelling concrete fracture," *Eng. Fract. Mech*., **65**, 283-298 (2000).
17. G. W. Ma, X. M. An, H. H. Zhang, and L. X. Li, "Modeling complex crack problems using the numerical manifold method," *Int. J. Fract.*, **156**, 21-35 (2009).
18. B.Goncalves da Silva and H. H. Einstein, "Modeling of crack initiation, propagation and coalescence in rocks," *Int. J. Fract.,* **182**, 167-186 (2013).
19. M. Wangen, "A 2D volume conservative numerical model of hydraulic fracturing," *Comput. Stuct.*, **182** , 448-458 (2017).
20. V. M. Yarushina, D. Bercovici, and M. L. Oristaglio, "Rock deformation models and fluid leak-off in hydraulic fracturing," *Geophys. J. Int*., **194**, 1514-1526 (2013).
21. N. Y. Wong, "Crack Coalescence in Molded Gypsum and Carrara Marble," (Ph.D.thesis) Massachusetts Institute of Technology (2008).
22. H. Q. Li and L. N. Y. Wong, "Influence of flaw inclination angle and loading condition on crack initiation and propagation," *Int. J. Solids Struct.,* **49**, 2482-2499 (2012).
23. B.Goncalves da Silva, "Modeling of Crack Initiation, Propagation and Coalescence in Rocks" (S.M. thesis), Massachusetts Institute of Technology (2009).